Carbon 227 (2024) 119252

Contents lists available at ScienceDirect

Carbon

journal homepage: www.elsevier.com/locate/carbon

The role of nanoporous carbon materials for thiophosphate-based all solid state lithium sulfur battery performance

Magdalena Fiedler [a,b], Martin A. Lange [c], Felix Hippauf [b], Susanne Dörfler [b,*], Holger Althues [b], Wolfgang G. Zeier [c,d], Stefan Kaskel [a,b]

[a] Chair of Inorganic Chemistry I, Technische Universität Dresden, Bergstraße 66, 01069, Dresden, Germany
[b] Fraunhofer Institute for Material and Beam Technology (IWS), Winterbergstraße 28, 01277, Dresden, Germany
[c] Institute of Inorganic and Analytical Chemistry, University of Münster, Correnstr. 30, 48149, Münster, Germany
[d] Institute of Energy and Climate Research (IEK), Helmholtz Institute Münster: Ionics in Energy Storage (IEK-12 / HI MS), Forschungszentrum Jülich, Germany

ARTICLE INFO

Keywords:
All-solid-state battery
Lithium-sulfur battery
Carbon
Ball milling
Thiophosphate electrolyte

ABSTRACT

Due to their high theoretical energy density, all solid state lithium sulfur batteries (LS-SSB) represent one of the most promising candidates for next-generation energy storage systems. Whilst high sulfur utilizations have been published for several cathode compositions and preparation methods in recent years, there is still a lack of clarity regarding the influence of the used carbon. Furthermore, LS-SSBs face challenges in up-scaling as the common preparation methods including high energy ball milling are time consuming, batch-wise and need high energy impact. In this study, high sulfur utilization >1600 mAh g_S^{-1} and reversibility with 80 % of initial discharge capacity after 60 cycles is achieved, using a more time-efficient preparation method with drastically lowered energy impact by selecting a suitable carbon. Additionally, the influence of the carbon nanostructure on the electrochemical performance is discussed. This study provides guidance in selecting nanostructured carbon materials to enable cost-efficient, up-scalable preparation methods for LS-SSBs without compromising on the excellent electrochemical performance.

1. Introduction

Lithium sulfur batteries (LSB) belong to the most promising candidates for next generation energy storage systems. Sulfur represents a low cost and light weight cathode active material, which is characterized by its high specific capacity of 1672 mAh g^{-1} and abundancy [1,2]. In combination with a metallic lithium anode, high gravimetric and volumetric energy densities can be reached, since lithium has a high specific capacity (3860 mAh g^{-1}) and low electrode potential (−3.04 V vs. SHE) [3,4]. However, LSB are facing several challenges, as they suffer from internal discharge due to the polysulfide shuttle and short circuits caused by lithium dendrite formation, resulting in low energy densities and insufficient long term stability [5–7]. Additionally, the flammability of liquid electrolytes is causing safety risks. All-solid-state LiS-batteries (LS-SSB) are considered as an alternative to overcome these challenges, since the solid electrolyte (SE) eliminates the polysulfide shuttle and improves the safety due to its non-flammability [8,9]. Nonetheless, the usage of SE causes new difficulties, for example in the cathode design. Sulfur has to be hosted within an electronically conductive (carbon-) matrix, since sulfur is an isolator [10–13]. Additionally, ionic pathways must be provided by the SE within the cathode. In conventional LiS-batteries, the porosity of the cathode is filled with liquid electrolyte and a swelling of the cathode occurs, ensuring the contact between sulfur and the ion-conducting electrolyte [14]. In contrast to that, the SE has to be well-distributed within the cathode to ensure ionic pathways A) through the cathode and B) within the composite particles to address the sulfur [7,15,16]. Furthermore, the SE has to be pressurized to cure grain boundaries. A volume change of occurs during the conversion of sulfur to lithium sulfide. This causes mechanical stress in the cathode, and leads to possible contact loss and thus lowered Li^+ ion transport in the cathode [17]. As known from the liquid LSB approach, the porous structure of carbon materials can compensate the volume change during the conversion reaction within the pore, overcoming mechanical stress and contact loss within the cathode. This is why the design of the cathode and the transport pathways becomes more important in comparison to "conventional" liquid systems. In recent years, the number of publications containing the keywords "all solid state lithium sulfur battery" has increased significantly. Still, there is a lack of clarity about

* Corresponding author.
E-mail address: susanne.doerfler@iws.fraunhofer.de (S. Dörfler).

https://doi.org/10.1016/j.carbon.2024.119252
Received 15 March 2024; Received in revised form 14 May 2024; Accepted 15 May 2024
Available online 16 May 2024

the influence of the cathode preparation method as well as the components, which are needed to improve the electrochemical performance in LS-SSB. Since the sulfur must be well distributed in an electronically conductive matrix, several strategies of C/S composite manufacturing are investigated to ensure electronic pathways. One common approach is to integrate the sulfur in a carbon material with high surface area/-porosity via melt infiltration (155 °C) or vapor deposition (300 °C), where the sulfur is well distributed and conducted at the surface of the carbon [18–21]. Another method is to prepare a network of covalent bonds between sulfur and a carbon backbone (sulfurized polyacrylonitrile, S-PAN), to ensure a homogenous distribution of sulfur and good electronic pathways [22–27]. Further concepts are to use sulfur in nm-scale as well as the application of conductive layers on these sulfur particles [22,28–32]. However, the latter approaches need high electrolyte to sulfur ratios, as the cathode porosity needs to be wetted with the liquid electrolyte, limiting the energy density. Besides the several methods of C/S composite preparation, various methods to obtain the cathode composite have been used. The most common preparation method for cathodes is ball milling in a planetary ball mill, and the majority of researchers are using "high energy ball milling" (HBM) with rotation speeds above 400 rpm for several hours [7,28,33–36]. The aim of HBM is to increase the formation of triple phase boundaries, as discussed in previous works. During ball milling, sulfur, solid electrolyte, and carbon are milled to small-scale particles, which form a homogenous cathode with low porosity. The transport of electrons and Li^+ ions to the insulating sulfur is taking place at the phase boundary between carbon, SE and/or sulfur/lithiumsulfide, leading to high active material utilization. Since the materials sulfur, solid electrolyte and carbon are exposed to harsh conditions during the ball milling, the particle morphology of the starting material is drastically altered, which is why the influence of different carbons and their structures is not fully understood yet. Even if high sulfur utilizations accompanied with high specific energies of the cathode can be realized, further challenges arise from HBM itself. The up-scaling of the preparation process in a planetary ball mill faces several problems, as this is a batch-wise preparation method and a production in kg-scale becomes challenging, considering the required size of the ball mill and production time. Hence, the preparation of LS-SSB-cathodes has to be adapted to enable continuous and scalable processes. It is necessary to reduce the required forces during the preparation of the cathode by choosing other materials/structures to A) reduce the required energy/time during cathode preparation, and B) find alternatives to the ball milling process.

First investigations with lowered energy impact were carried out by Hayashi et al. [20,37]. They investigated a so called "low energy ball milling" (LBM) preparation method, which was still carried out in a planetary ball mill, but with lower rotation speed (300 rpm) and time (15 min instead of several hours). Their work demonstrated that a comparable electrochemical performance can be reached by using low mechanical impact during mixing, which openes up new approaches of the cathode design. Furthermore, they observed a different electrochemical behavior, depending on the initial porous structure of the carbon. It was demonstrated that micro- and mesoporous carbons enable a better sulfur utilization in comparison to acetylene black, which has a lower pore volume.

Based on this work, different carbons were investigated in this study to get deeper insights into the influence of the carbon structure on the electrochemical performance of the LiS-batteries. Therefore, six commercially available carbons with different pore structures and pore volumes were deployed as carbon material for LS-SSB cathodes and electrochemically analyzed. We tried to correlate these findings with structural and morphological analysis such as nitrogen physisorption and FIB-sections of the carbon and understand how it changes during the mixing process. Based on these investigations we aim to define parameters and guidelines for the right choice of carbon that enables a high-energy cathode for LS-SSB under more economic and efficient processing conditions than HBM does.

2. Results and discussion

As carbon materials, six different commercially available carbons were chosen. They can be separated into templated carbons (TC) CNovel-MH (TC1) and CNovel-MJ (TC2), and four activated carbons (AC), named AC TTT (AC1), ASAC 30 (AC2), Norit SX Super S (AC3) and YP 50F (AC4). The aim was to investigate different carbon structures as well as various particle sizes and porosities. Since an influence on the carbon structure is assumed to be induced by the cathode preparation via LBM, the structure of the carbons before and after LBM was explored.

2.1. Carbon characterization

2.1.1. Nitrogen physisorption measurement

To investigate the influence of the carbon structure on the electrochemical performance of LS-SSBs, nitrogen physisorption measurements were performed before and after LBM of the pure carbons (Fig. 1). Based on IUPAC classification of isotherms, TC 1 and TC2 display a Type IV isotherm (mesopores). AC1 and AC2 demonstrate a mixture of Type IV and Type I isotherm (mesopores and micropores). The slope of the isotherm below p/p_0 of 0.5 is significantly steeper for AC2 compared to AC1, thus a higher mesopore volume and wider pore size distribution is observed for AC2. AC3 and AC4 exhibit a Type I isotherm (micropores) [38]. The highest pore volume was observed for the mesoporous carbon TC2 (2.05 g cm^{-3}), followed by TC1 and the meso/microporous carbon AC2 (both 1.8 g cm^{-3}). A lower pore volume was noticed for the second meso/microporous carbon AC1 (0.8 g cm^{-3}). The lowest pore volume was distinguished for the microporous carbons AC3 and AC4 (0.7 g cm^{-3}). All carbons are characterized by a high specific BET surface area of more than 1000 $m^2\ g^{-1}$.

After LBM, it can be noticed that the porosity of the carbons with high mesopore volume (TC1, TC2 and AC2) is decreased. The shape of the isotherms aligns with the isotherms of the microporous carbons, which were less affected by the LBM. The lowered mesopore volume was also noticeable in the pore size distribution, displayed in Fig. S1 and Fig. S2. We conclude that the mesopores create a more unstable carbon framework, which is easily destroyed during LBM. The microporous domains of the carbon framework exhibit a higher stability and remain intact during LBM. The porosity of the microporous carbons AC1, AC3 and AC4 is not affected during LBM significantly.

2.1.2. Particle size distribution before and after ball-milling

Besides physisorption measurements, the particle size distribution (PSD) of the carbons was investigated before and after LBM, as shown in Fig. 2 and Fig. S3. Before ball milling, differences between the carbons are noticeable. Whilst AC3 and AC4 display a sharp, monomodal PSD, a less defined PSD was noticed for AC1, but in the same range of particle sizes below 10 μm. In contrast to that, TC1 and AC2 demonstrate a wide distribution consisting of bigger particles between 20 μm and 120 μm. For TC2 a trimodal particle size distribution was observed before ball milling.

During LBM, the particle size distribution of the carbons is lowered and a monomodal PSD is observed for all carbons, as displayed in Fig. 2B. The particle sizes of the carbons TC1, TC2, AC1 and AC2 is significantly lowered during LBM. The activated carbons AC3 and AC4, which showed a sharp PSD at low particle sizes for the raw materials, are less affected during LBM. All carbons demonstrate a monomodal PSD, where the major amount of the particles is in the range of 1 μm up to 10 μm (Fig. 2C). TC1, TC2 and AC1 demonstrate a narrow PSD, whilst AC2, AC3 and AC4 exhibit broader PSD. The D_{50} and D_{90} values can be sorted as follows: AC1 < TC1 = TC2 < AC4 < AC2 = AC3.

2.1.3. Scanning electron microscopic analysis (SEM) before and after ball-milling

SEM images of the carbons before (raw) and after LBM are displayed in Fig. 3. As already observed in PSD measurements (Fig. 2), TC1 is

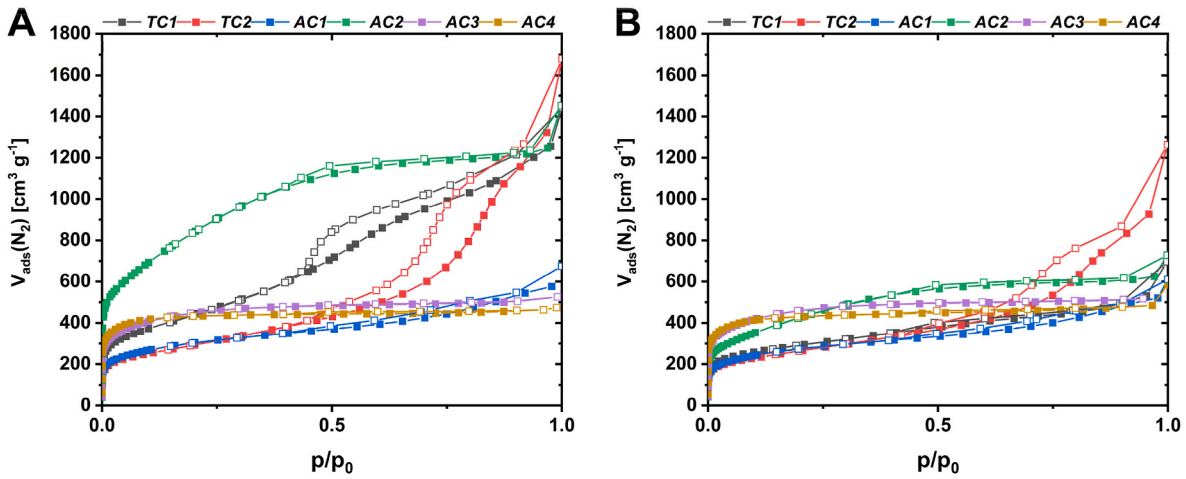

Fig. 1. Nitrogen adsorption isotherms (77 K) of the used carbons: A) before LBM, B) after LBM.

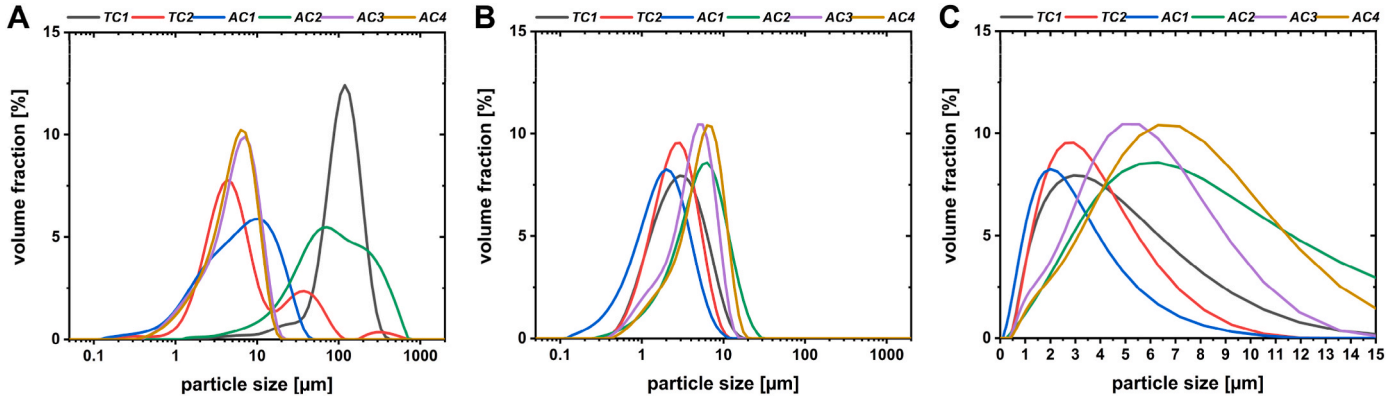

Fig. 2. Particle size distribution of the pure carbons: A) differential distribution before ball milling, B) differential distribution after ball milling (logarithmic scale), C) differential distribution after ball milling (linear scale).

characterized by large particles of up to 100 µm, which are also displayed in the SEM image (Fig. 3A). Further, a macroporous structure is observed, which is not obvious from nitrogen physisorption measurements (Fig. 1). In contrast to that, smaller but compact particles up to 10 µm are noticeable for the second template based carbon TC2. For AC2, again larger particles up to 30 µm with a porous morphology are visible, correlating well to the physisorption and PSD data. For the meso/microporous carbons AC1, AC3 and AC4, several particles in different size below 10 µm can be noticed. In contrast to TC1, TC2 and AC2, the microporous carbons powders are characterized by a sharp particle morphology.

A certain impact of the LBM procedure on the particle size and shape can be seen for the carbons TC1, TC2, AC1 and AC2, where the particle size is reduced significantly. Furthermore it can be noticed, that the particles of AC3 and AC4 seem to be more stable against the energy impact during LBM, since the particle size is less affected by the LBM process. The carbon characterization demonstrated that the carbons are specified by different porosities, particles sizes or rather shapes. Furthermore, the impact of the LBM was different, leading to different carbon structures after ball milling (Fig. S2). After melt infiltration of the sulfur and mixing with solid electrolyte, the electrochemical performance of the cathodes was evaluated and is discussed in the following section.

2.2. Electrochemical performance

As an example for LS-SSB, the voltage profile of TC1 is displayed in Fig. 4A (additional voltage profiles can be found in Fig. S4). In this study, InLi alloy was used as anode, which accounts for the lowered voltage by 0.62 V vs. Li^+/Li. During discharge, the formation of two voltage plateaus can be observed. The first plateau is present at a voltage of 1.45 V vs. InLi. A second plateau is pronounced at a slightly decreasing voltage below 1.4 V vs. InLi until the cut-off voltage of 1 V is reached. During charge, only one plateau between 1.6 V and 1.8 V is detected. The voltage profile demonstrates a high sulfur utilization of 1545 mAh g_S^{-1} in the second discharge compared to the theoretical value of 1672 mAh g_S^{-1}. The conversion mechanism of S_8 to Li_2S in LS-SSBs has not been fully understood yet, in contrast to conventional liquid LSBs. There, polysulfides are dissolved in the electrolyte leading to a two-step conversion of long-chain and short-chain polysulfides, which results in two voltage plateaus. The presence of dissolved polysulfides leads to internal discharge caused by the polysulfide shuttle leading to a moderate sulfur utilization of conventional liquid LSBs. By contrast, in LS-SSBs the mobility of emerging sulfide species, and hence the shuttle, is reduced to zero. In addition, the Li^+-selectivity of the solid electrolyte and high transfer numbers result in a high utilization of sulfur in comparison to liquid systems, when decent triple phase boundaries between carbon, sulfur and SE are enabled. The observation of two voltage plateaus during discharging leads to the assumption that a stepwise reaction is also taking place in LS-SSBs. Y. Xiao et al. reported in 2020 that in the solid-state electrolyte, the sulfur cathode was reduced to long-chain polysulfide (S_6^{2-}) at the initial stage of the first discharge process and was gradually reduced to mid-chain polysulfide (S_4^{2-}), short-chain polysulfide (S_2^{2-}), and Li_2S. The conclusions were obtained by using XANES

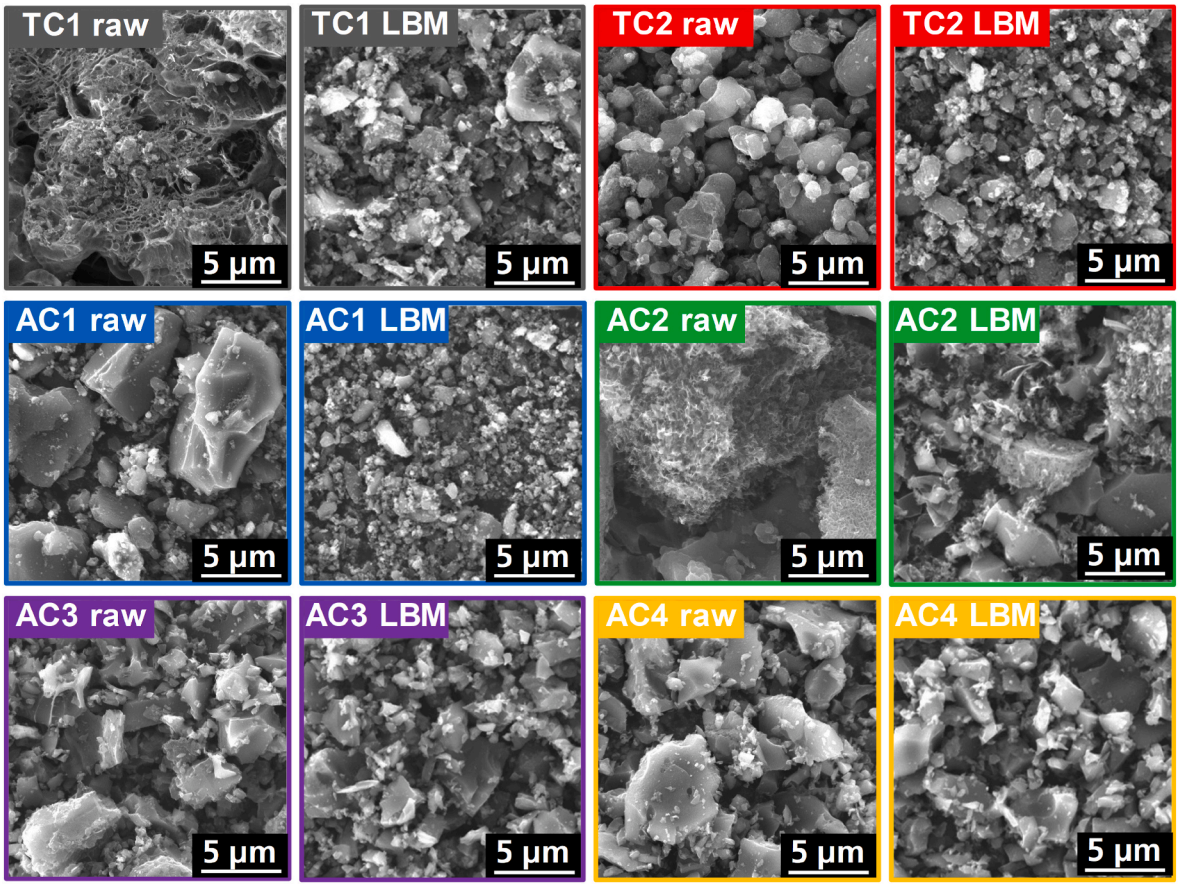

Fig. 3. SEM images of the raw carbons and after ball milling (LBM).

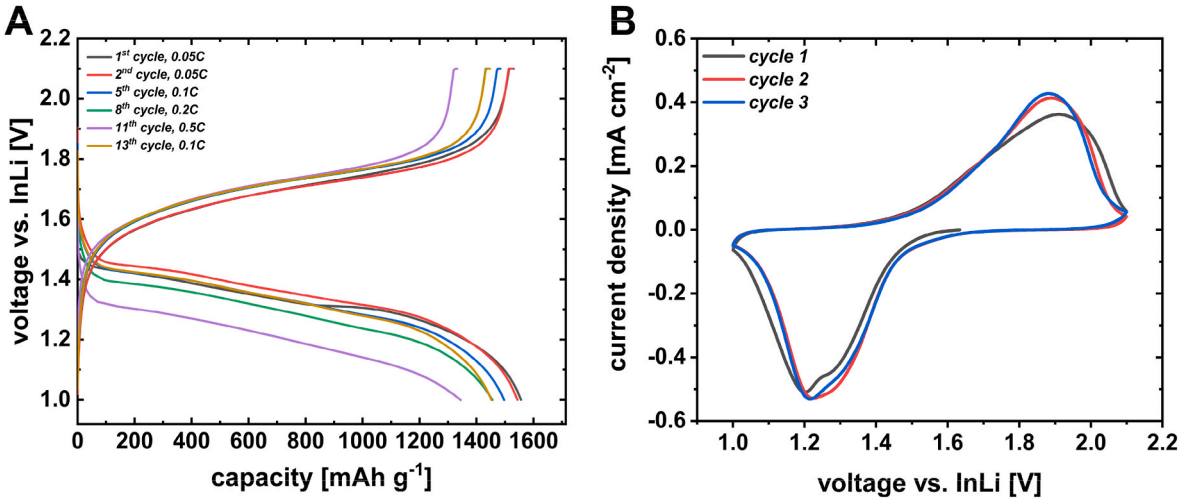

Fig. 4. A) Voltage profile of the cathode with TC1 as carbon material (1.5 mg_S cm^{-2}, 25 °C), B) cyclic voltammogramm of TC1 (1.75 mg_S cm^{-2}, 25 °C).

and the achieved capacities were quite low – hence, there is a certain dubiety if these findings are completely transferable to our results [39]. Previous work of Cao et al. assumed that the conversion takes place with Li_2S_2 as intermediate species in a solid-solid conversion reaction, corresponding to the observed voltage profiles [40].

In the second cycle (red), a slightly lower discharge capacity is observed, which differs from our previous work, where the investigated cathodes were prepared via HBM. During HBM, all components in general and the solid electrolyte in particular are amorphized and triple phase boundaries are formed [41]. As a result, the solid electrolyte becomes more electrochemically active and is decomposed during cycling (especially in the first cycle), leading to a higher capacity and contributing to the overall capacity [42–44]. Since this behavior was not observed for the LBM cathode, we conclude that the solid electrolyte particles remain intact and are not decomposed during cycling. After the first three cycles, where a high sulfur utilization above 1550 mAh g_S^{-1} is observed, the C-rate was increased to 0.1C for charge and discharge (Fig. 4A). The increased C-rate results in a slightly lowered, reversible capacity of 1495 mAh g_S^{-1} and the average voltage is lowered to 1.32 V vs. InLi during discharging and increased to 1.73 V vs. InLi during

charging. The discharge capacity is slightly lowered in the subsequent cycles at higher C-rates, 1450 mAh g_S^{-1} (93 % of initial discharge capacity) at 0.2C. The discharge capacity is further decreased to 1350 mAh g_S^{-1} (86 %) at the highest C-rate of 0.5C accompanied by an average discharge voltage of 1.21 V vs. InLi. After the rate test, the C-rate was lowered to 0.1C in cycle 13, and the capacity is recuperated, demonstrating a similar voltage profile as observed in the 5th cycle, which was also conducted at 0.1C and discharge capacity 1450 mAh g_S^{-1} (93 %). Thus, the capacity loss during increasing C-rates is mainly caused by kinetic limitations while irreversible capacity losses can be ruled out. Besides galvanostatic cycling, cyclovoltammetry was carried out, displayed in Fig. 4B. An anodic peak is observed at 1.2 V vs. InLi during the first cycle (grey) and a shoulder at 1.28 V is noticeable. The shoulder of the anodic peak is subsequently less pronounced in the second and third cycle. The potential of the anodic peak is slightly shifted towards higher potentials of 1.22 V in the third cycle, but the current density of the anodic peak maintains constant at −0.50 mA cm^{-2}. Additionally, one cathodic peak occurs at 1.91 V vs. InLi in the first cycle with a current density of 0.36 mA cm^{-2}. The cathodic peak is slightly shifted towards 1.89 V during the second cycle and 1.88 V in the third, accompanied by an increased current density of 0.41 mA cm^{-2}. The redox potential of the sulfur conversion in the all-solid-state battery can be calculated from the average potential of the anodic and cathodic peak. Following, the redox potential is E = 1.55 V vs. InLi (2.17 V vs. Li/Li^+). By comparison of the cyclovoltammetry and the voltage curves from galvanostatic cycling at the same current (0.05C), an overpotential during charging and discharging is observed. The average potential during charging and discharging the cell at 0.05C was 1.34 V respectively 1.71 V, as discussed earlier. Hence, a voltage deviation from the redox potential of 0.21 V during discharging and 0.16 V during charging was noticed.

The comparison of the electrochemical performance of the different carbons is displayed in Fig. 5. TC1, which was discussed in Fig. 4 before, demonstrates an outstanding rate test performance and high reversibility. A high reversibility and low linear degradation was observed for TC1, a template carbon with high mesopore volume and a relatively low particle size of 3 µm after LBM resulting in 1250 mAh g_S^{-1} (80 %) after 60 cycles. Furthermore, a high coulombic efficiency of 100.05 % is observed during the long-term performance test. A different electrochemical performance was noticed for the other carbons. TC2, AC1, AC2 and AC3 demonstrate both a lower rate performance and long-term stability. All these carbons demonstrate a high sulfur utilization during the first discharge of more than 1450 mAh g_S^{-1}, which is subsequently lowered during the first cycles. The difference in the addressability of sulfur for each carbon becomes more prominent at higher C-rates. Whilst 93 % of initial discharge capacity are observed for TC1 at 0.2C, the capacity is lowered to 87 % for TC2, ~70 % for AC1 and AC3, and 63 % for AC2. At the highest C-rate of 0.5C, more than 50 % of the initial discharge capacity are extracted for TC2 and AC3, and ~30 % for AC1 and AC2. After the rate test, an increase of the discharge capacity can be observed for all carbons, resulting in 89 % for TC2 and more than 70 % for AC1, AC2 and AC3. A subsequent degradation is observed during the long-term performance test, resulting in capacities between 38 % and 48 % for the described carbons after 60 cycles. In contrast to the aforementioned carbons, a poor electrochemical performance was observed for AC4, a microporous carbon with 6–7 µm particle size after LBM. A low sulfur utilization of 526 mAh g_S^{-1} is reached during the first discharge, which is significantly lowered to 400 mAh g_S^{-1} during the first three cycles. The capacity is further lowered to 100 mAh g_S^{-1} at 0.1C, before the capacity approaches zero at the higher C-rates. After 60 cycles, only 50 mAh g_S^{-1} (10 %) can be utilized. In general, differences in the electrochemical performance in dependence of the used carbon were noticed. Whilst TC1 demonstrates a high reversibility and outstanding electrochemical performance, higher dependency of the C-rates and higher degradation during the long-term performance test is present for the carbons TC2, AC1, AC2 and AC3. In summary, carbons with a certain mesoporous structure and lower average particle sizes (TC 1 and TC 2) perform better than microporous carbons with higher particle size after ball-milling which will be further discussed in the following paragraph (especially under 2.3.2). In contrast to the other carbons, a significantly lower sulfur utilization is noticed for AC4.

2.3. The role of nanocarbon structure for electrochemical performance

As discussed in 2.2., differences in the electrochemical active material utilization were observed when using different carbon materials. In this section, different electrochemical and morphological methods were combined to obtain further insights into the carbon structure itself and the resulting cathode. The aim was to elaborate a trend or characteristic parameter of the carbon/cathode to create the most holistic view on the mechanisms of sulfur conversion within these LBM derived cathodes. Therefore, the data of the different analysis methods was ordered with decreasing electrochemical performance (capacity in cycle 13) in the

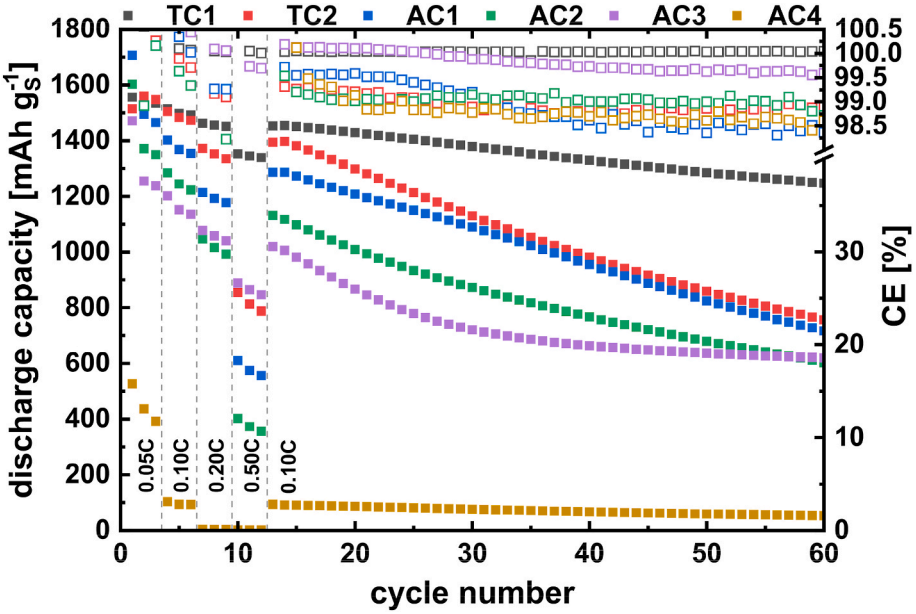

Fig. 5. Comparison of the cycle performance of the tested cathodes (1.5 mg_S cm^{-2}, 25 °C).

following section, starting with the highest sulfur utilization (TC1) at the left, to AC4, which demonstrated the lowest capacity, at the right.

2.3.1. Partial conductivities of the sulfur/carbon/SE cathodes

Since the cathodes with the different carbons showed different electrochemical performance and different dependencies on the C-rate, electronic and ionic conductivities of cathodes were measured to receive further insights on the kinetic limitations on the transport processes within the cathodes. A common approach to investigate cathode performance more deeply is to measure partial conductivities by direct current polarization (DCIR) or impedance spectroscopy (EIS) and link it with the tortuosity or morphology of the cathode [33,45].

It can be seen, that the electronic conductivities are in a range between 9.4 mS cm^{-1} (AC1) up to 45.7 mS cm^{-1} (TC2) (Fig. 6). TC1 has the second lowest electronic conductivity with 13.4 mS cm^{-1}, followed by AC4 (15.3 mS cm^{-1}), AC3 (24.9 mS cm^{-1}) and AC2 (27.5 mS cm^{-1}). The difference between all cathodes is significant if displayed on the logarithmic scale. Hence, no relation between the electronic conductivity and the electrochemical performance was observed, since TC2 and AC1 showed comparable electrochemical performances but the highest and lowest electronic conductivity. The opposing trend was observed for the ionic conductivity. There, TC2 is characterized with the lowest conductivity (3.1 µS cm^{-1}), whereas AC1 shows a higher ionic conductivity (6.3 µS cm^{-1}). Whilst the sulfur utilization of the cathodes AC2 (4.9 µS cm^{-1}), AC3 (10.1 µS cm^{-1}) and AC4 (19.3 µS cm^{-1}) was lower, the ionic conductivity is higher. This observation leads to the conclusion that the partial conductivities through the cathodes are no significant parameter for the resulting electrochemical active material utilization of the cathode vs. LiIn anode in this range of loading (2.5 mAh cm^{-2}) [46]. As long as a certain critical value is exceeded, the kinetic limitations within the cathode can be conducted to the sulfur conversion reaction itself, not to the transport kinetics of electrons and Li^+ ions within the cathode.

2.3.2. Detailed porosity analysis of the investigated carbon materials as conductive host material for sulfur and lithium sulfide

Since partial conductivities of the cathode cannot explain electrochemical performance, we take a deeper look on the porosity of the carbon itself. As the porosity of the carbons was discussed generally before (chapter 2.1.1), a more detailed analysis of the porous structure was carried out and is discussed in the following. Therefore, the pore volume, average pore size and ratio of sulfur to pore volume was chosen as parameter, displayed in Fig. 7.

By consideration of Fig. 7A, no remarkable trend or relation between the total pore volume and the electrochemical performance can be observed, neither before or after ball milling. The total pore volume after ball milling varies for all carbons between 0.7 and 0.9 $cm^3\ g^{-1}$, except TC2 which has a noticeably higher total pore volume of 1.42 $cm^3\ g^{-1}$. Since the total pore volume is comparable for five out of the six used carbons after LBM, a more detailed analysis of the pore volume is shown in Fig. 7B, where it was divided into micropore and mesopore volume. Both TC samples as well as AC1 and AC2 are characterized by a higher mesopore volume compared to the micropore volume. The micropore volume is below 0.3 $cm^3\ g^{-1}$ for these carbons, whilst the mesopore volume varies between 0.5 $cm^3\ g^{-1}$ respectively 1.3 $cm^3\ g^{-1}$ for TC2, which had the exceptional high total pore volume compared to the other carbons. The carbons AC3 and AC4 demonstrate a higher micropore volume in comparison to the mesopore volume, accompanied with the lowest (initial) sulfur utilization (Fig. 5). During LBM, the carbon particle size is lowered and the mesopore volume is decreased, accompanied by a lowered surface area of the carbons as the carbon agglomerates are disintegrated. Furthermore, the average pore size was determined by calculating the median of the pores after DFT analysis (Fig. 7C). It can be seen, that the average pore sizes of TC1, TC2 and AC1 are in the same range about 6 nm, accompanied by a comparable electrochemical performance with high sulfur utilization at low C-rates. AC2, where a slightly lowered sulfur utilization was demonstrated, is characterized by an average pore size of 3 nm, whereas the microporous carbons AC3 and AC4 display a low average pore size below 1 nm and were characterized with a poor addressability of sulfur. Given that a volume expansion during conversion of sulfur to lithium sulfide is expected, we calculated the ratio of the sulfur species volume (sulfur and lithium sulfide) to pore volume after LBM for each carbon (Fig. 7D and Equation S1). The V_S/V_{pore} of the respective carbon demonstrates that sufficient pore volume is present to host 60 wt% of sulfur within the pores for all carbons except AC4. Hence, a defined distribution of the sulfur within the pores, a good electric contact and electrochemical accessibility of the sulfur is presumed after melt infiltration. During discharge, a conversion of sulfur to lithium sulfide occurs, resulting in a volume expansion. The V_{Li2S}/V_{pore} ratio is higher than one for each carbon except TC2. It can be concluded that the porous structure of the carbon cannot compensate the active material's volume expansion during conversion. Following, breathing behavior and mechanical stress within the cathode is expected during conversion reaction, leading to possible contact loss and degradation of the cathode.

2.3.3. Detailed analysis of the cathode density and morphology of the grain boundaries

Based on the analysis of the partial conductivities and carbon structure, we were not able to point out an explicit correlation between

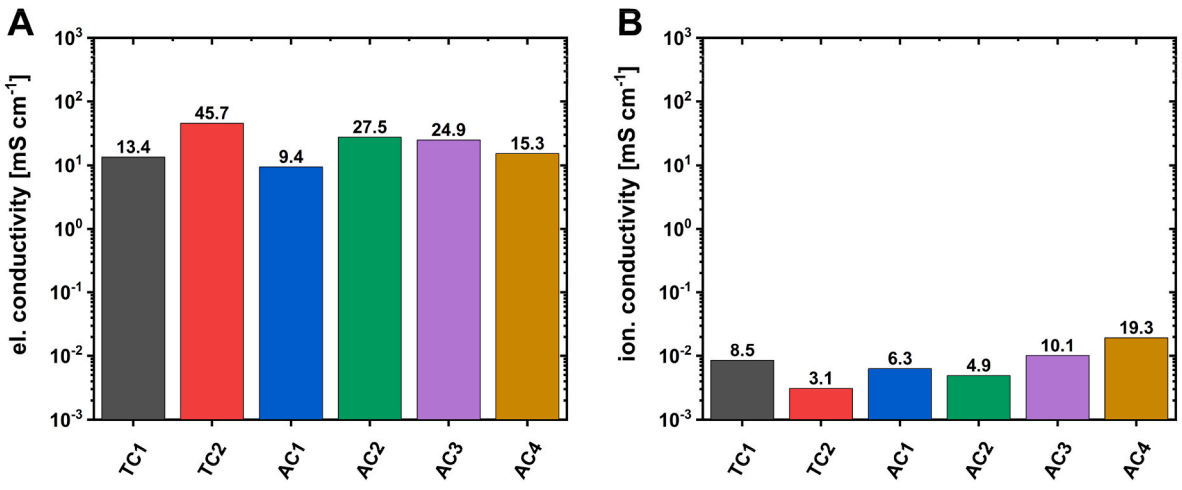

Fig. 6. Partial conductivities of the cathodes: A) electronic conductivity; B) ionic conductivity.

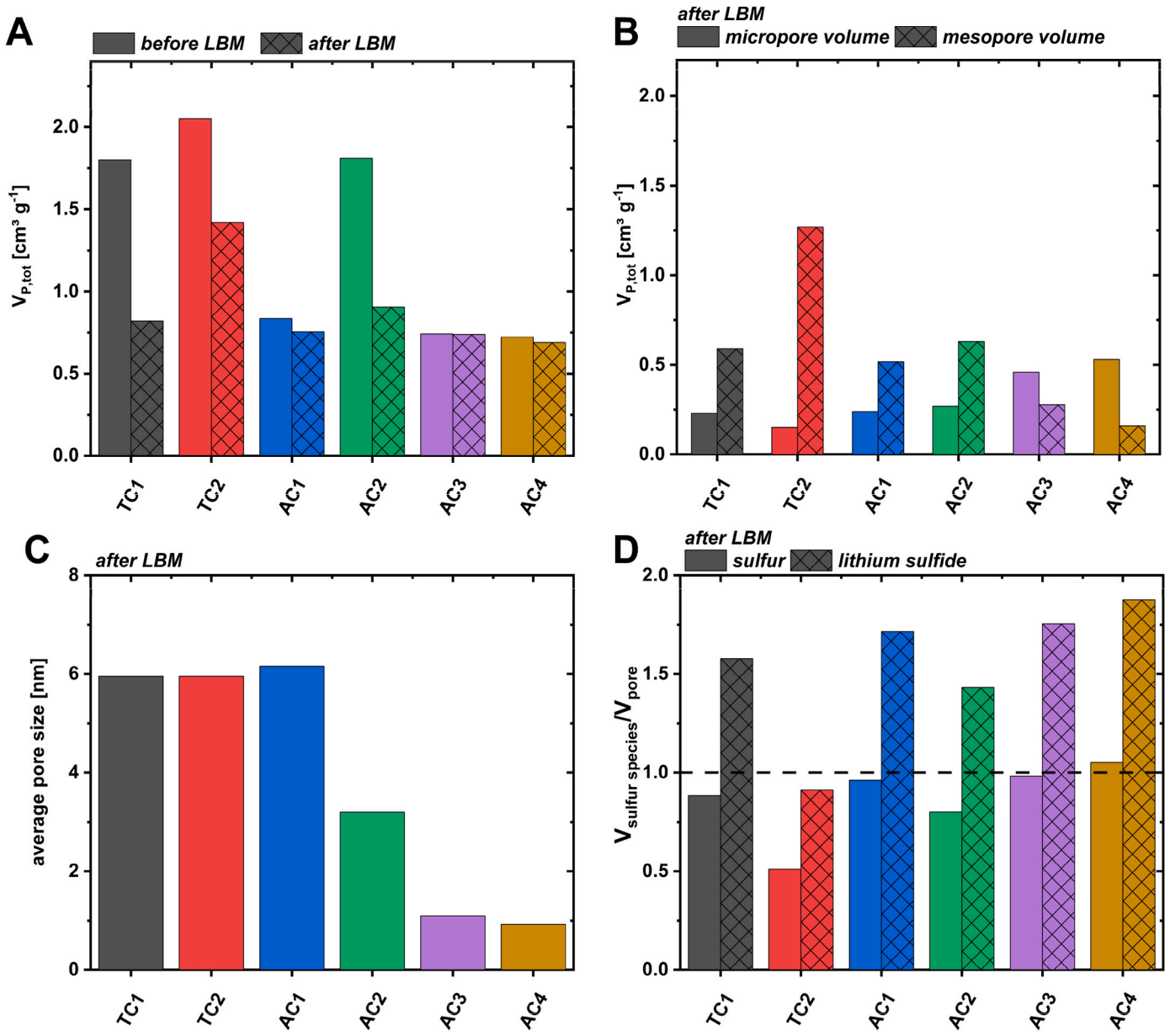

Fig. 7. Detailed analysis of nitrogen physisorption measurements: A) total pore volume, B) micro- and mesopore volume after LBM, C) average pore size after LBM, D) ratio of sulfur species volume to pore volume after LBM.

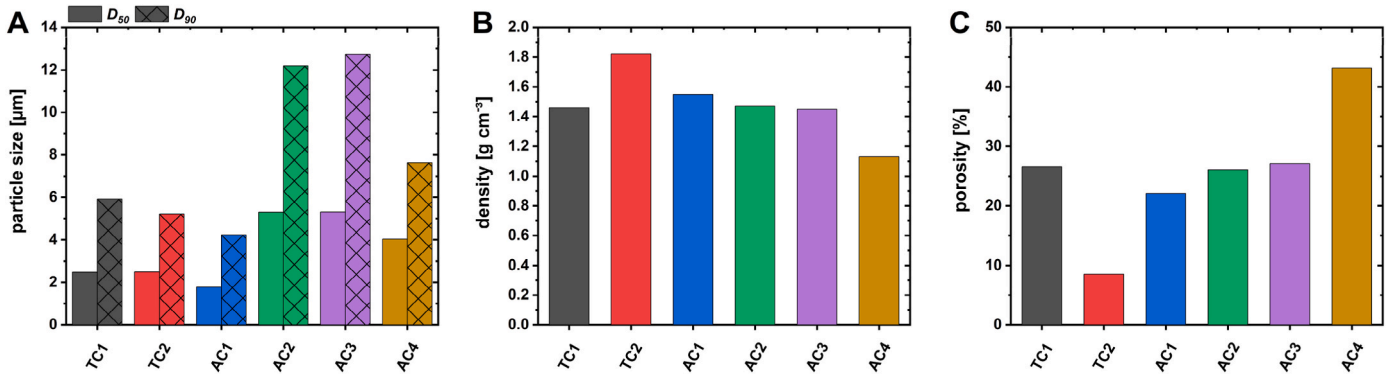

Fig. 8. A) the particle size distribution of the carbons after LBM; B) density of the pressurized cathodes; C) porosity of the pressurized cathodes.

the carbon and the resulting electrochemical performance. Following, the morphology of the cathode was examined to receive a general impression of the cathode. The particle size distribution of the pure carbons after LBM is displayed in Fig. 8A. The carbons can be divided into two groups: TC1, TC2 and AC1 are composed of smaller particles, with a D_{50} of approximately 2 µm and D_{90} below 6 µm. The second group (AC2, AC3 and AC4) are consisting of bigger particles with a D_{50} above 4 µm and D_{90} between 8 and 13 µm. In combination with the electrochemical performance, it was observed that the samples with the smaller PSD after LBM (TC1, TC2 and AC1) showed a better electrochemical performance than the second group consisting of bigger particles. Hence it was concluded, that smaller particles enhance a better utilization of sulfur in LS-SSBs.

After analyzing the pristine carbons, the entire cathodes containing carbon, sulfur and solid electrolyte were investigated, in order to obtain insights into the morphology in the final pressurized cell. Fig. 8B displays the density of the cathodes after pressurization. It can be seen that the density varies between 1.1 g cm^{-3} up to 1.8 g cm^{-3}. For all-solid-state electrodes, the density or rather the porosity of the electrodes is essential as pores in the electrodes act as isolator, where the ionic and electronic pathways are hindered, leading to kinetic limitations within the electrode. At the same time, certain porosity is required to enable Li_2S transformation and the accompanied volume expansion. The porosity is displayed in Fig. 8C (Equation S2). For the cathodes containing TC1, AC1, AC2 and AC3, the values of the porosity are in the same range between 22 and 27 %. The cathode with TC2 exposes the lowest porosity of 9 %. In contrast to that, the porosity of AC4 is 43 %, which is eight times higher than for TC2 and higher compared to the literature, where values between 5 % up to 20 % are discussed [15,17,33,47]. Based on the different porosities after pressurization, it was presumed that the compressibility of the respective cathodes/carbon particles has to be different. Consequently, FIB-SEM measurements were carried out before and after pressurization to obtain a detailed image of the cathodes and their morphology (**Fig. 9**/S5). In general, solid electrolyte particles appear brighter (light grey) than the carbon particles (dark grey) and no sulfur crystals were found in SEM images. A comparable morphology of the cathode can be noticed for TC1 and TC2. The SEM-image displays solid electrolyte particles, where the majority is smaller than 1 µm. In vicinity of the solid electrolyte particles, few dark grey spots in the range of 1–2 µm can be noticed, representing intact primary carbon particles. Furthermore, the solid electrolyte particles are surrounded by a middle-grey matrix.

This middle-grey matrix is attributed to a homogenous carbon sulfur composite/SE morphology with particles in sub-µm-scaled area, but not nm-scale, as observed after HBM. Based on these findings, we presume that the carbon particles are compressed during LBM. Hence, the carbon structure collapses, leading to a homogenous, dense cathode of solid electrolyte particles surrounded by the carbon/sulfur matrix. Following, a good contact of carbon/sulfur/SE is ensured at the grain boundaries, resulting in a high electrochemical active material utilization. The cathodes AC1 and AC2 demonstrate a slightly different morphology. In contrast to the TC samples, several primary carbon particles (dark) up to 3 µm are present in the cathode. Nonetheless, solid electrolyte particles in µm-scale are still noticeable, as well as the sub-µm-scaled matrix between the SE and bigger carbon particles. The structure of the cathodes AC1 and AC2 appears comparable to TC1 and TC2, but rougher/in a higher range of particle sizes. It can be concluded that the solid electrolyte is well compressed during pressurization, followed by reduced grain boundaries. The higher amount of carbon matrix, which still appears as defined particles, is less affected during pressurization than the TCs, resulting in an inhomogenous/rougher morphology of the cathode and cracks within the cathode due to possible tensions within the cathode caused by the inhomogeneous pressurization. Hence, the contact between solid electrolyte and carbon/sulfur-particles is lowered, leading to the observed lower electrochemical addressability of the sulfur. AC3 demonstrates a different morphology, where no SE particles are observed. Furthermore, larger carbon particles up to 5 µm are present, surrounded by a non-defined, homogenous matrix, which can be interpreted as solid electrolyte. The cathode of AC4 differs strongly from the other electrodes. In this case, carbon sulfur particles and solid electrolyte particles can clearly be separated from each other, and the amount of intact carbon particles is remarkably higher. Both particle species are present next to each other without a transformation due to the pressurization of the cathode. Furthermore, the carbon particles are present as comparably larger particles up to 6 µm. These darker carbon particles are surrounded by solid electrolyte particles, but interstices are present in between, leading to the high porosity, which was observed before. The insufficient contact between solid electrolyte and carbon/sulfur particles leads to the discussed higher resistances and reduced ionic and electronic conductivity trough the cathode (see 2.3.1). In summary, the electronic as well as the ionic pathways are hindered due to the particular shape of the cathode and the present grain boundaries. Consequently, the sulfur cannot be addressed sufficiently, resulting in the poor electrochemical performance that was observed for AC4 (Fig. 5).

The different mechanical behavior of the carbons during LBM can be

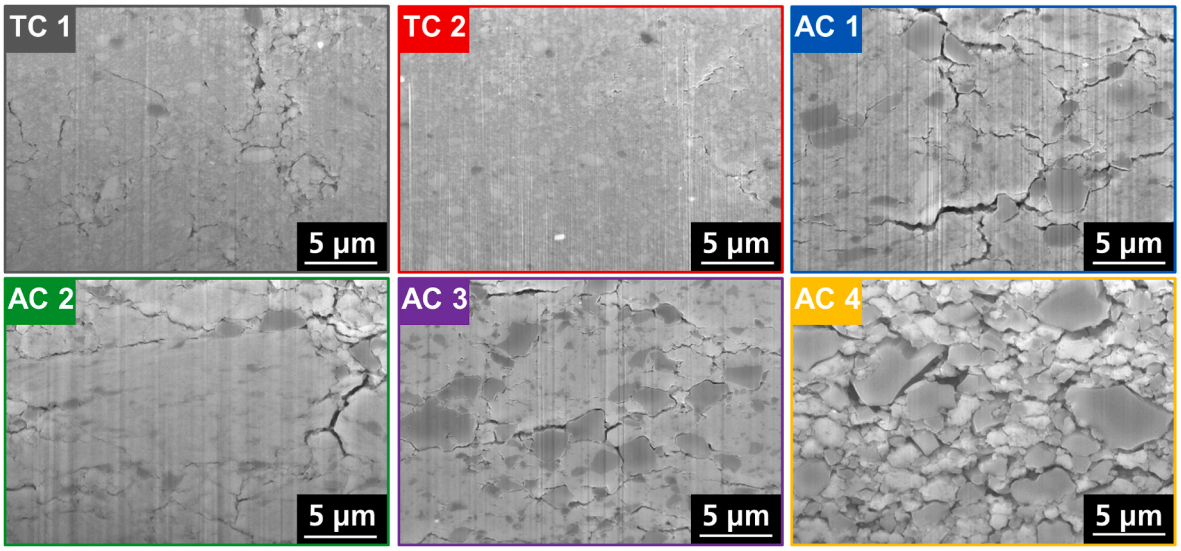

Fig. 9. FIB-SEM images of the cathodes after pressurization at 360 MPa.

correlated to the carbon structure. For TC1, TC2 and AC1 small particles size distributions were observed. Furthermore, TC1, TC2, AC1 and AC2 were characterized by a higher mesopore than micropore volume. We conclude that the presence of mesopores and macropores (which were observed in Fig. 3) leads to a fragile carbon structure. During LBM, most carbon particles disintegrates, resulting in a homogenous cathode structure embedded in a sub-µm-scaled matrix, ensuring sufficient contact at the grain boundaries and high addressability of sulfur. In contrast to that, AC3 and AC4 were characterized by a higher micropore than mesopore volume, leading to small average pore sizes. Furthermore, the particle size was higher compared to TC1, TC2 and AC1. As a result, the carbon particles demonstrated a higher stability, as observed in FIB-SEM images. Nonetheless, differences in compressibility and electrochemical performance between AC3 and AC4 were noticed. We assume that the carbon particles of the AC4 are mechanically more stable than AC3, which is why they are still clearly present after the pressurization of the cathode. Hence, an inhomogeneous cathode with interstices between SE and carbon particles was observed in the FIB-SEM, corresponding to the low density. As a result, insufficient contact between SE and carbon particles is present, leading to the low addressability of sulfur. Based on the aforementioned results of average pore size, particle size and cathode morphology, we concluded the following transport mechanism of Li^+-ions and conversion of sulfur to Li_2S (Fig. 10).

At 100 % SOC, the sulfur is hosted within the pores, where the pores of the activated carbon with low average pore size (upper line) are filled to 100 %, whilst the pores of the carbons with larger average pore size (e.g. template-based carbons) are not filled to 100 %. Subsequently, during discharging, the sulfur is converted to Li_2S, where the Li^+-ions are transported by the solid electrolyte as well as by the intermediate species (Li_2S_2 and Li_2S), resulting in high initial discharge capacities. During charging, the cathode (full conversion of sulfur to Li_2S), elemental sulfur is formed again. As noticeable in Fig. 10, we assume that the sulfur is built at the interface between Li_2S and solid electrolyte, consequently, sulfur is growing towards the inside of the pore, clogging its entrance. Hence, the slit pores of the activated carbons with small pore diameter are blocked by the non-ion-conductive sulfur after a critical SOC, leading to blocked pores and hence a lower Li_2S/sulfur utilization. In contrast to that, a good ionic conductivity is provided within the cathodes of the template-based carbons, where solid electrolyte is surrounded by the sub-µm-scaled matrix and Li^+-ion pathways are shortened. Consequently, the conversion of sulfur to lithium sulfide and back to sulfur is not limited due to insufficient ionic conductivity and blocked pores. This conclusion is consistent with the observed partial conductivities. These partial conductivities could not explain the electrochemical behavior, since they represent the conductivity through the entire cathode, not the conductivities at the reaction fronts, which are more crucial for kinetics of the conversion reaction.

2.3.4. GITT measurements of selected cathodes

In order to shed light into the kinetic limitations of the (dis)charging process, GITT measurements were carried out at 25 °C and 60 °C to confirm our assumed Li^+-ion transport mechanism within the cathode (Fig. 11, S6).

Besides the cathodes TC1 and AC4, a cathode consisting of a hierarchical carbon and prepared via HBM was investigated. As published previously, this cathode is characterized by triple phase boundaries, where the particles are disintegrated to nm-scale. Thus, differences in the Li^+ ion transport are expected, which should be observed in the GITT measurement. As discussed previously, the evolution of an ion-blocking area was expected for AC4, resulting in higher overpotentials. For TC1, where a more homogenous sub-µm-scaled structure was observed, we expect the overpotential to be lower and to start increasing at a high SOC. The HBM cathode with nm-scale triple phase boundaries should not be affected by ion-blocking sulfur areas during charging, resulting in lower overpotentials. At 60 °C the differences between the three cathodes becomes more prominent, which is why they are discussed in this section. For TC1, two OCV plateaus are observed during discharging and charging as observed previously (Fig. 4). The upper voltage plateau (2.0 V vs. InLi) is characterized by an overpotential of 0.7 V. At 25 % DOD, the OCV voltage drops to 1.5 V and the overpotential is lowered to 0.4 V at the beginning of the second discharge plateau. Subsequently, the overpotential is rising until the voltage drop approaches 0 V at 100 % DOD. During charging, the overpotential is rising in the first steps, before remaining constant at 0.1 V until a SOC of 40 %. Afterwards, the overpotential is increasing to 0.7 V at a SOC of 75 %. At this SOC, the OCV voltage is increasing and a second charge plateau is observed at 2.0 V. The overpotential is constantly increasing until 2.5 V at 100 % SOC. The rising overpotential is mainly related to the rising R_{diff} during charging (Fig. 11B). For AC4, only one OCV-plateau was observed at 1.5 V (Fig. 11C). Again, the overpotential was subsequently increasing, starting at 0.45 V at 0 % DOD to 1 V at 100 % DOD. During charging, two regions of overpotential are observed. Until 40 % SOC, the overpotential remains constant at 0.1 V, comparable to the overpotential of TC1. With increasing SOC, the overpotential is rising to 1 V between 50 % and 90 % SOC. Subsequently, the overpotential is increasing significantly, until the cut-off voltage of 10 V is reached at 98 % SOC. Again, the rising overpotential can mainly be related to the increasing R_{diff} (Fig. 11D).

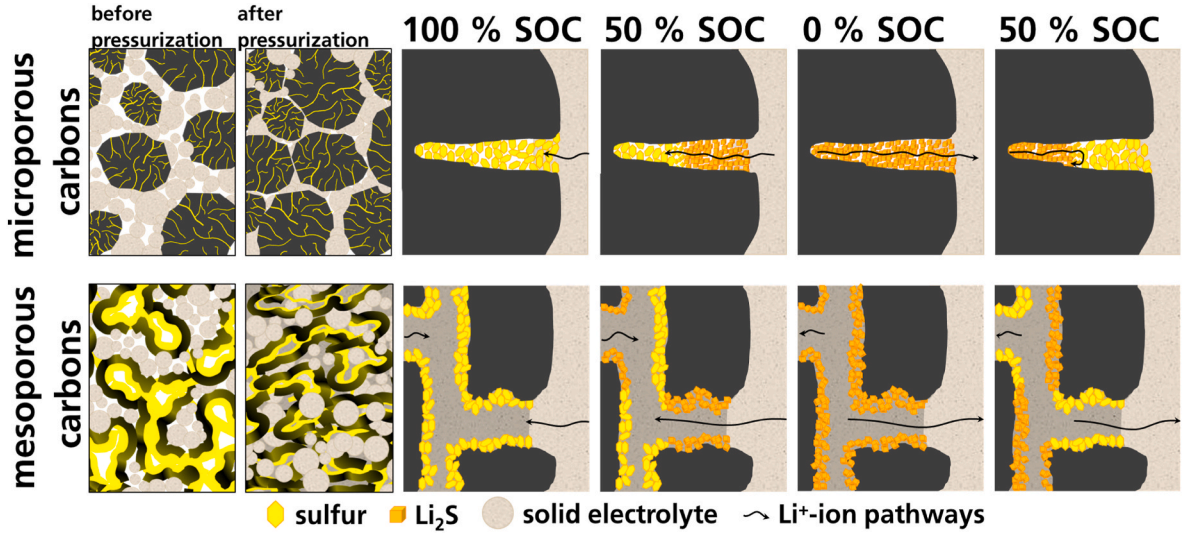

Fig. 10. Assumed transport of Li^+-ions within the pores of carbon.

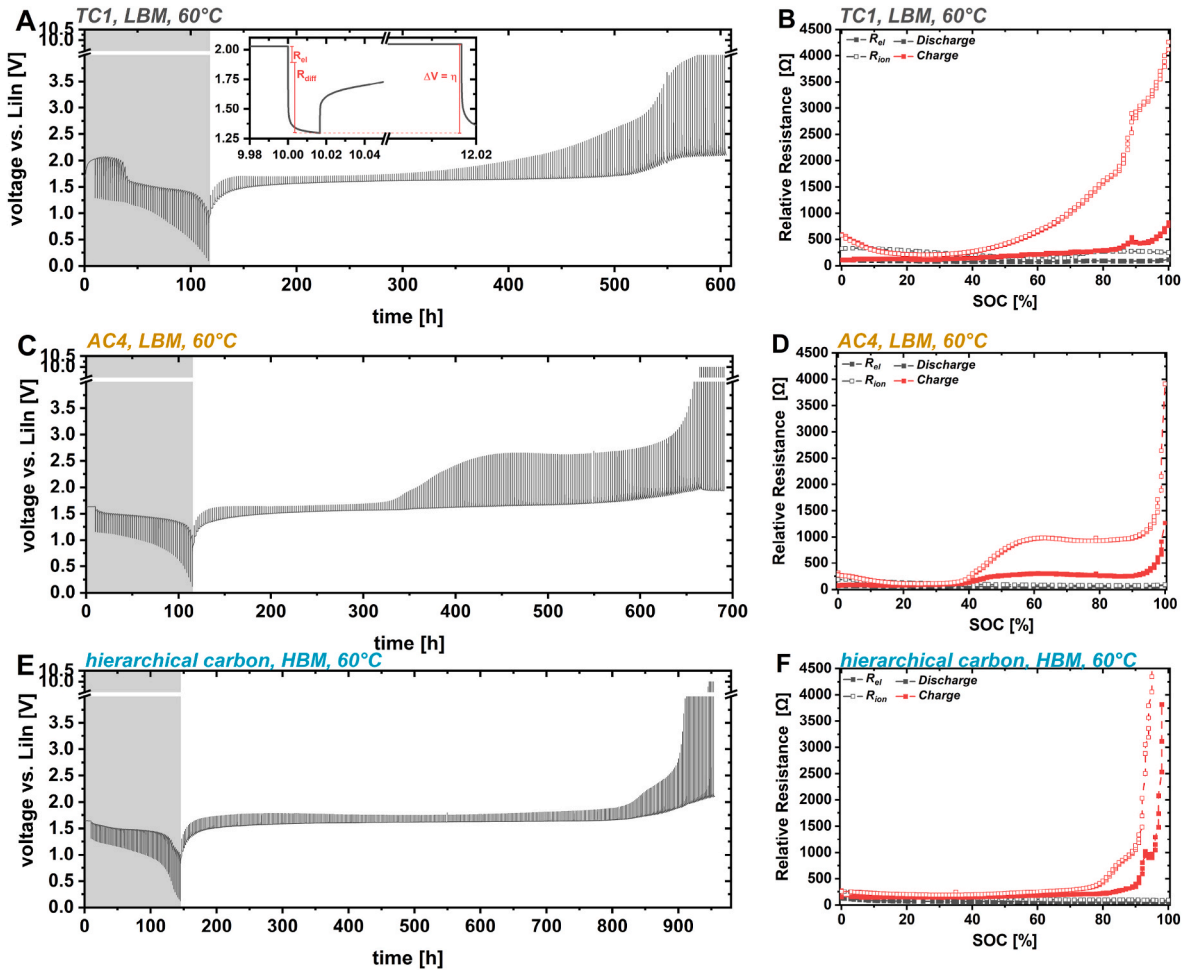

Fig. 11. GITT-measurements and calculated resistances of the tested cathodes at 60 °C: A + B) TC1; C + D) AC4; E + F) hierarchical carbon.

The third cathode (HBM) is characterized by a discharge behavior, where only one plateau was observed and the overpotential is subsequently increasing until 100 % DOD (Fig. 11E). During charging, only one plateau is observed, accompanied by a low, constant overpotential of 0.2 V. The low resistances R_{diff} and R_{el} remain constant until 80 % SOC, before increasing significantly. The differences in the evolution of overpotential during cycling, confirm our aforementioned assumption of Li^+-ion transport mechanism within the LBM cathodes. It was noticed, that the overpotential in AC4 starts to increase significantly at an SOC of 40 %, whereas the overpotential of TC1 reaches comparable values at 75 % SOC. The increase of the overpotential at lower SOCs confirms our theory that the pores of AC4 are blocked by the sulfur, which is why the kinetics of the conversion reaction are reduced and the Li_2S cannot be addressed sufficiently. Since the HBM cathode is characterized by particles and triple phase boundaries on nm-scale, the CAM is well distributed, ensuring short electronic and ionic pathways, followed by the low overpotential (enhanced kinetics) even at high SOCs.

3. Conclusion

Six different commercially available carbons and their influence on the electrochemical performance of all-solid-state LiS-batteries were investigated in this work. It was demonstrated that a high sulfur utilization >1600 mAh g_S^{-1} is achievable by processing electrodes with sulfidic electrolyte in a more efficient/economic process than the common HBM. Furthermore, high reversible capacities >800 mAh g_S^{-1} at a C-rate of 0.5C were obtained, as well as up to 80 % of initial discharge capacity after 60 cycles. The carbon, which is used as sulfur host, shows a significant impact on the electrochemical performance in LS-SSBs. Generally, the template-based carbon cathodes show a comparably high electrochemical active material utilization and rate capability. Activated carbons, however, led to different performance, depending on their pore structure. The activated carbons with higher pore volume and average pore size achieved a better electrochemical performance than the activated carbons with low pore volume. The electronic and ionic conductivities within the cathode sheet cannot be considered as a decisive parameter, since the distribution of pathways at the grain boundaries on a nm-scale become more crucial. FIB-SEM analysis showed remarkable differences in the cathode morphology, which differs for cathodes prepared via HBM, as shown in our previous work. In this work, a sub-µm-scaled cathode structure with particles between 100 nm and 1 µm was observed, and the amount of the sub-µm-scaled structure differs for each carbon. With increasing evolvement of this sub-µm-scaled fine structure, an improved sulfur utilization and rate performance was observed. By consideration of the electrochemical data and carbon/cathode analysis, following conclusions can be stated: The type of carbon (template based/activated carbon) shows an influence on the compressibility of the cathodes, leading to comparably more densified cathodes, directly influencing the electrochemical performance. The presence of mesopores, which results in higher pore volume and average pore sizes, leads to a more fragile carbon structure, compared to microporous carbons. Hence, neither the original mesopore structure nor the macrostructure is preserved, as it is disintegrated into smaller particles during LBM, resulting in high densities of the cathodes, which ensures sufficient electronic and ionic pathways. In these types of carbons, the material only acts as a precursor and its disintegration

pathway and processing conditions determine the final performance of the cathode.

The analysis of six different carbons as conductive material in LS-SSBs proved, that the pore and particle structure is directly linked with the electrochemical performance. We demonstrated that the properties of the carbon, especially the mechanical stability of the carbon particles, lead to different behavior during ball milling. The varying impact of the ball milling procedure on the carbon particles resulted in different cathode morphologies and consequently in different electrochemical performance.

With selecting a suitable carbon, high sulfur utilizations and rate performance can be achieved without using time-consuming HBM as batch-wise synthesis method. Hence, the energy impact on the cathode materials can be reduced due to the selection of a porous carbon with high average pore size and fragile structure. The decreased required energy impact enables new preparation strategies, as the ball milling could be substituted by more cost-efficient, up-scalable processes.

4. Materials and methods

Physisorption measurement: For physisorption measurements, using a BELSORP instrument (Japan) at 77 K, the carbon samples were activated at 200 °C for 12 h. To calculate the specific surface areas Brunauer-Emmett-Teller (BET) method was used in the range of relative pressure from $p/p_0 = 0.05–0.3$. The total pore volume was determined at relative pressure of $p/p0 = 0.99$. Pore size distributions were calculated using quenched solid density functional theory (QSDFT) method for carbon (slit/cylindrical/spherical pores) using the adsorption branch. Based on the pore size distribution, the cumulative pore volume below pores of 2 nm was defined as the micropore volume. Following, the mesopore volume was calculated as difference between total pore volume and micropore volume.

FIB-SEM: A scanning electron microscope JSM-6060 (JEOL, Japan) was used for SEM analysis with an accelerating voltage of 10 kV.

Particle size distribution: A Mastersizer 3000 (Malvern Pananalytical, Ltd) at a dispersion pressure of 4 Bar was used to obtain the particle size distribution of the used carbons before and after ball milling.

Preparation of cathode composite: The preparation of the cathode composites was performed in an argon-filled glovebox. In a first step, sulfur (Sigma Aldrich) and carbon were mixed in weight ration 3:2 in a mortar. Following a sulfur infiltration step was carried out at 155 °C for 1 h under argon atmosphere. In a second step, 150 mg of the prepared carbon sulfur composite and 150 mg solid electrolyte (Li_6PS_5Cl, D_{50} = 0.6 μm) were added to a ball mill jar (50 mL, 60 g $Zr0_2$ balls with 1 mm diameter) and ball milled for 15 min at a rotation speed of 300 rpm using a planetary ball mill (PM100, Retsch GmbH).

Preparation of the manual dry-film cathodes: To prepare a free-standing cathode dry-film, 0.5 wt% of PTFE were added to the prepared cathode composite. Afterwards, the blend was transferred in a heated mortar and sheared, until a single cathode flake was formed. The flake was rolled out on a heated plate to a thickness of ~50 μm and the obtained dry film was stomped out to the desired diameter of the cathodes.

Assembly of solid-state pressurized cell: For the assembly of the lab-scale cells an InLi alloy was used as anode. Therefore, an Indium foil (100 μm thick, 13 mm diameter) was placed on the stainless-steel current collector. Subsequently, a lithium foil (50 μm thickness) with the same diameter was placed on top. Subsequently, 150 mg of solid electrolyte were filled on top of the anode and distributed evenly with a spatula to prepare the separator layer. In a next step, the solid electrolyte was pelletized un-der moderate pressure followed by the assembly of the as prepared dry-film cathode on top of the solid electrolyte layer. The prepared cell was pressed in a hydraulic press under 110 bar for 30 s, placed in an outer steel case and tensed at 3.5 Nm.

4.1. Electrochemical characterization

GCPL: Galvanostatic measurements were carried at a battery tester CTS-Lab (BaSyTec, Germany) at constant temperature of 25 °C. The performed rate test between 1 V and 2.1 V vs. InLi consisted of three cycles at rising C rates, starting at C/20 to C/10, C/5, C/2. During charging, the C rate was kept at C/20 during the first three cycles and at C/10 afterwards, using an additional CV-step after reaching the upper potential limit. Following the rate performance test, the long-term performance was tested for more than 50 cycles at C/10.

DCIR: To investigate the electrical conductivity, the dry-film cathodes were stomped to a diameter of 13 mm and placed between two stainless steel current collectors. DC polarization was carried out using a VSP-300 (Bio-Logic, France) by applying alternating currents (100 mA, -100 mA, 200 mA, - 200 mA, 240 mA, 240 mA) for 30 s. Ionic conductivity was carried out under ion-blocking conditions using a stack of In/InLi|Li_6PS_5Cl|S–C-SE|Li_6PS_5Cl|In/InLi. 80 mg of argyrodite Li_6PS_5Cl were employed as an electron-blocking electrode. First, a layer of solid electrolyte was placed in the cell, densified by hand-pressing, before the dryfilm cathode was placed on top, followed by the final solid electrolyte layer. The so assembled cell was pressed for 3 min under 3 tons of uniaxial pressure. Afterwards 9 mm diameter Indium foil (100 μm thickness, chemPur, 99.995 %) followed by freshly pressed Lithium discs (1.5 mg, 100 μm thickness) were applied to both solid electrolyte sides. The effective conductivities of the cathode composites were evaluated by DC polarization. Under electron-blocking conditions, constant potentials of 5 mV, 10 mV, 15 mV, 20 mV, 25 mV and 50 mV were employed and the current value after 6 h of equilibration was determined.

CV: Cyclovoltammetry was carried out at a scan rate of 0.015 mV/s, corresponding to 0.05C. The voltage range was set between 1 V and 2.1 V vs. InLi.

GITT: After 5 h resting step, half cells were discharged and charged once, using galvanostatic intermittent titration technique. A current of 1C was applied for 1 min, followed by a 2 h resting step in a voltage range between 1 V and 2.1 V vs. InLi.

CRediT authorship contribution statement

Magdalena Fiedler: Writing – original draft, Visualization, Data curation, Conceptualization. **Martin A. Lange:** Writing – review & editing, Data curation. **Felix Hippauf:** Writing – review & editing, Methodology, Conceptualization. **Susanne Dörfler:** Writing – review & editing, Project administration, Funding acquisition. **Holger Althues:** Writing – review & editing, Supervision, Funding acquisition. **Wolfgang G. Zeier:** Writing – review & editing. **Stefan Kaskel:** Writing – review & editing, Supervision.

Declaration of competing interest

The authors declare the following financial interests/personal relationships which may be considered as potential competing interests:

Susanne Doerfler reports financial support was provided by German Federal Ministry of Education and Research Bonn. If there are other authors, they declare that they have no known competing financial interests or personal relationships that could have appeared to influence the work reported in this paper.

Acknowledgements

This research and development results are funded by the German Federal Ministry of Education and Research (BMBF) within the SoLiS project (Grant No. 03XP0395) and AReLiS-3 project (03XP0595).

Appendix A. Supplementary data

Supplementary data to this article can be found online at https://doi.org/10.1016/j.carbon.2024.119252.

References

[1] J.B. Robinson, K. Xi, R.V. Kumar, A.C. Ferrari, H. Au, M.-M. Titirici, A. Parra-Puerto, A. Kucernak, S.D.S. Fitch, N. Garcia-Araez, et al., JPhys Energy 3 (2021) 31501.
[2] Z. Shi, M. Li, J. Sun, Z. Chen, Adv. Energy Mater. 11 (2021).
[3] W. Xu, J. Wang, F. Ding, X. Chen, E. Nasybulin, Y. Zhang, J.-G. Zhang, Energy Environ. Sci. 7 (2014) 513–537.
[4] X.-Z. Fan, M. Liu, R. Zhang, Y. Zhang, S. Wang, H. Nan, Y. Han, L. Kong, Chin. Chem. Lett. 33 (2022) 4421–4427.
[5] Z.-C. Lv, P.-F. Wang, J.-C. Wang, S.-H. Tian, T.-F. Yi, J. Ind. Eng. Chem. 124 (2023) 68–88.
[6] Q. Shao, S. Zhu, J. Chen, Nano Res. 16 (2023) 8097–8138.
[7] S. Bandyopadhyay, B. Nandan, Mater. Today Energy 31 (2023) 101201.
[8] C. Wang, J. Liang, Y. Zhao, M. Zheng, X. Li, X. Sun, Energy Environ. Sci. 14 (2021) 2577–2619.
[9] S. Ohno, W.G. Zeier, Acc. Mater. Res. 2 (2021) 869–880.
[10] Y. de Luna, M. Abdullah, S.N. Dimassi, N. Bensalah, Ionics 27 (2021) 4937–4960.
[11] N.H.H. Phuc, K. Hikima, H. Muto, A. Matsuda, Crit. Rev. Solid State Mater. Sci. (2021) 1–26.
[12] E. Umeshbabu, B. Zheng, Y. Yang, Electrochem. Energy Rev. 2 (2019) 199–230.
[13] S. Randau, D.A. Weber, O. Kötz, R. Koerver, P. Braun, A. Weber, E. Ivers-Tiffée, T. Adermann, J. Kulisch, W.G. Zeier, et al., Nat. Energy 5 (2020) 259–270.
[14] F. Schmidt, S. Ehrling, K. Schönherr, S. Dörfler, T. Abendroth, H. Althues, S. Kaskel, Energ. Tech. 10 (2022).
[15] L. Froboese, J.F. van der Sichel, T. Loellhoeffel, L. Helmers, A. Kwade, J. Electrochem. Soc. 166 (2019) A318–A328.
[16] K. Nie, Y. Hong, J. Qiu, Q. Li, X. Yu, H. Li, L. Chen, Front. Chem. 6 (2018) 616.
[17] X. Yang, J. Luo, X. Sun, Chem. Soc. Rev. 49 (2020) 2140–2195.
[18] A.S. Alzahrani, M. Otaki, D. Wang, Y. Gao, T.S. Arthur, S. Liu, D. Wang, ACS Energy Lett. 6 (2021) 413–418.
[19] L.-P. Hou, H. Yuan, C.-Z. Zhao, L. Xu, G.-L. Zhu, H.-X. Nan, X.-B. Cheng, Q.-B. Liu, C.-X. He, J.-Q. Huang, et al., Energy Storage Mater. 25 (2020) 436–442.
[20] T. Ando, Y. Sato, T. Matsuyama, A. Sakuda, M. Tatsumisago, A. Hayashi, J. Ceram. Soc. Japan 128 (2020) 233–237.
[21] M. Nagao, Y. Imade, H. Narisawa, T. Kobayashi, R. Watanabe, T. Yokoi, T. Tatsumi, R. Kanno, J. Power Sources 222 (2013) 237–242.
[22] Q. Zhang, N. Huang, Z. Huang, L. Cai, J. Wu, X. Yao, J. Energy Chem. 40 (2020) 151–155.
[23] M. Li, J.E. Frerichs, M. Kolek, W. Sun, D. Zhou, C.J. Huang, B.J. Hwang, M. R. Hansen, M. Winter, P. Bieker, Adv. Funct. Mater. 30 (2020) 1910123.
[24] T. Zhu, X. Dong, Y. Liu, Y.-G. Wang, C. Wang, Y.-Y. Xia, ACS Appl. Energy Mater. 2 (2019) 5263–5271.
[25] X. Zhu, L. Wang, Z. Bai, J. Lu, T. Wu, Nano-Micro Lett. 15 (2023) 75.
[26] S. Luo, E. Zhao..
[27] Z. Sun, Y. Hu, F. Qin, N. Lv, B. Li, L. Jiang, Z. Zhang, F. Liu, Sustain. Energy Fuels 5 (2021) 5603–5614.
[28] Q. Han, X. Li, X. Shi, H. Zhang, D. Song, F. Ding, L. Zhang, J. Mater. Chem. A 7 (2019) 3895–3902.
[29] B. Fan, Z. Guan, L. Wu, S. Zhang, M. Tan, Z. Luo, X. Zhang, H. Ma, B. Xue, J. Am. Ceram. Soc. 106 (2023) 5781–5794.
[30] X. Sun, Q. Li, D. Cao, Y. Wang, A. Anderson, H. Zhu, Small (2021) 2105678.
[31] M. Yamamoto, S. Goto, R. Tang, K. Nomura, Y. Hayasaka, Y. Yoshioka, M. Ito, M. Morooka, H. Nishihara, T. Kyotani, ACS Appl. Mater. Interfaces 13 (2021) 38613–38622.
[32] X. Yao, N. Huang, F. Han, Q. Zhang, H. Wan, J.P. Mwizerwa, C. Wang, X. Xu, Adv. Energy Mater. 7 (2017) 1602923.
[33] G.F. Dewald, S. Ohno, J.G.C. Hering, J. Janek, W.G. Zeier, Batter. Supercaps 4 (2021) 183–194.
[34] B. Ding, J. Wang, Z. Fan, S. Chen, Q. Lin, X. Lu, H. Dou, A. Kumar Nanjundan, G. Yushin, X. Zhang, et al., Mater. Today 40 (2020) 114–131.
[35] D. Wang, L.-J. Jhang, R. Kou, M. Liao, S. Zheng, H. Jiang, P. Shi, G.-X. Li, K. Meng, D. Wang, Nat. Commun. 14 (2023) 1895.
[36] H. Yuan, H.-X. Nan, C.-Z. Zhao, G.-L. Zhu, Y. Lu, X.-B. Cheng, Q.-B. Liu, C.-X. He, J.-Q. Huang, Q. Zhang, Batter. Supercaps 3 (2020) 596–603.
[37] A. Sakuda, Y. Sato, A. Hayashi, M. Tatsumisago, Energy Technol. 7 (2019) 1900077.
[38] M. Thommes, K. Kaneko, A.V. Neimark, J.P. Olivier, F. Rodriguez-Reinoso, J. Rouquerol, K.S. Sing, Pure Appl. Chem. 87 (2015) 1051–1069.
[39] Y. Xiao, K. Yamamoto, Y. Matsui, T. Watanabe, A. Sakuda, K. Nakanishi, T. Uchiyama, A. Hayashi, S. Shingubara, M. Tatsumisago, et al., ACS Appl. Energy Mater. 4 (2021) 186–193.
[40] D. Cao, X. Sun, F. Li, S.-M. Bak, T. Ji, M. Geiwitz, K.S. Burch, Y. Du, G. Yang, H. Zhu, Angew. Chem. 62 (2023) e202302363.
[41] M. Fiedler, S. Cangaz, F. Hippauf, S. Dörfler, T. Abendroth, H. Althues, S. Kaskel, Adv. Sustain. Syst. 7 (2023).
[42] S. Ohno, C. Rosenbach, G.F. Dewald, J. Janek, W.G. Zeier, Adv. Funct. Mater. 31 (2021).
[43] T. Hakari, Y. Sato, S. Yoshimi, A. Hayashi, M. Tatsumisago, J. Electrochem. Soc. 164 (2017) A2804–A2811.
[44] S. Wang, M. Tang, Q. Zhang, B. Li, S. Ohno, F. Walther, R. Pan, X. Xu, C. Xin, W. Zhang, et al., Adv. Energy Mater. 11 (2021).
[45] P. Minnmann, L. Quillman, S. Burkhardt, F.H. Richter, J. Janek, J. Electrochem. Soc. 168 (2021) 40537.
[46] R. Bradbury, G.F. Dewald, M.A. Kraft, T. Arlt, N. Kardjilov, J. Janek, I. Manke, W. G. Zeier, S. Ohno, Adv. Energy Mater. 13 (2023).
[47] A. Bielefeld, D.A. Weber, J. Janek, J. Phys. Chem. C 123 (2019) 1626–1634.